The Astronomical Journal, 172:302 (7pp), 2026 December https://doi.org/10.3847/1538-3881/aeaff7
© 2026. The Author(s). Published by the American Astronomical Society.
OPEN ACCESS

Spatial Profiles of 3I/ATLAS CN and Ni Outgassing from Keck/KCWI Integral Field Spectroscopy

Willem B. Hoogendam[1,7], Benjamin J. Shappee[1], James J. Wray[1,2], Bin Yang[3], Karen J. Meech[1], Christopher Ashall[1], Dhvanil D. Desai[1], Kyle Hart[1], Jason T. Hinkle[1,4,5,8], Andrew Hoffman[1], Esther M. Hu[1], David O. Jones[6], Kyle Medler[1], and Cameron M. Pfeffer[1]
[1] Institute for Astronomy, University of Hawai'i, 2680 Woodlawn Drive, Honolulu, HI 96822, USA
[2] School of Earth and Atmospheric Sciences, Georgia Institute of Technology, 311 Ferst Drive, Atlanta, GA 30332, USA
[3] Instituto de Estudios Astrofísicos, Facultad de Ingeniería y Ciencias, Universidad Diego Portales, Santiago, Chile
[4] Department of Astronomy, University of Illinois Urbana-Champaign, 1002 West Green Street, Urbana, IL 61801, USA
[5] NSF-Simons AI Institute for the Sky (SkAI), 172 E. Chestnut Street, Chicago, IL 60611, USA
[6] Institute for Astronomy, University of Hawai'i, 640 N. A'ohoku Place, Hilo, HI 96720, USA
Received 2026 May 5; revised 2026 October 1; accepted 2026 October 2; published 2026 November 5

Abstract

Cometary activity from interstellar objects provides a unique window into the environs of other stellar systems. We report blue-sensitive integral field unit (IFU) spectroscopy of the interstellar object 3I/ATLAS from the Keck II–mounted Keck Cosmic Web Imager on 2025 August 24 UT. We confirm the previously reported CN and Ni outgassing and, for the first time, present the radial profiles of Ni and CN emission in 3I/ATLAS. We find characteristic *e*-folding radii of 593.7 ± 14.8 km for Ni and 841.0 ± 15.4 km for CN; this suggests that the Ni emission is more centrally concentrated in the comet's nucleus and favors hypotheses involving easily dissociated species, such as metal carbonyls or metal–polycyclic aromatic hydrocarbon (PAH) molecules. Additional integral field spectroscopy after perihelion will provide an ongoing opportunity to determine the evolution of the radial distributions of species in the interstellar comet 3I/ATLAS.

Unified Astronomy Thesaurus concepts: Interstellar objects (52); Comets (280); Comet volatiles (2162); Small Solar System bodies (1469); Astrochemistry (75); Planetesimals (1259)

1. Introduction

Interstellar objects (comets and asteroids that pass through the solar system on hyperbolic orbits) offer a rare (e.g., A. Do et al. 2018) window into the chemical and physical processes behind small bodies in other stellar systems (e.g., D. Jewitt & D. Z. Seligman 2023; A. Fitzsimmons et al. 2024). Recently, the discovery of 3I/ATLAS (L. Denneau et al. 2025; D. Z. Seligman et al. 2025; J. Tonry et al. 2025) by the Asteroid Terrestrial-impact Last Alert System (ATLAS; J. L. Tonry et al. 2018; J. Tonry et al. 2025) has caused considerable excitement in the astronomical community. 3I/ATLAS is the third object of this type, following 1I/'Oumuamua (K. J. Meech et al. 2017) and 2I/Borisov (G. Borisov et al. 2019).

One avenue to understanding these objects is from cometary activity or lack thereof. This activity results from solar radiation heating the surface-layer materials (e.g., F. W. Bessel 1836; F. L. Whipple 1950, 1951; J. J. Cowan & M. F. A'Hearn 1982). When a comet warms, its volatile ices sublimate, lifting dust off the surface and creating the coma. Sunlight excites these gas molecules, which then reemit light by resonance fluorescence—revealing the composition of the volatiles. For solar system comets, this provides a window into the primordial composition of the solar system (e.g., D. Bodewits et al. 2024). Interstellar objects enable similar studies for otherwise inaccessible stellar systems (e.g., D. Jewitt & D. Z. Seligman 2023).

The first two interstellar objects differed in their activity. No outgassing or coma was directly observed for 1I/'Oumuamua, despite extensive observations (e.g., D. Jewitt et al. 2017; K. J. Meech et al. 2017; Q.-Z. Ye et al. 2017; D. E. Trilling et al. 2018; 'Oumuamua ISSI Team et al. 2019). However, the only possible explanation for the nongravitational acceleration of 1I/'Oumuamua was due to outgassing by CO or CO_2 (M. Micheli et al. 2018). On the other hand, 2I/Borisov had outgassing activity and a dusty coma (A. Fitzsimmons et al. 2019; D. Jewitt & J. Luu 2019; G. Cremonese et al. 2020; P. Guzik et al. 2020; M.-T. Hui et al. 2020; Y. Kim et al. 2020; A. J. McKay et al. 2020; Q. Ye et al. 2020; B. Yang et al. 2021). The gas and dust of 2I/Borisov showed features in common with solar system comets, including CN (A. Fitzsimmons et al. 2019; C. Opitom et al. 2019), C_2 (H. W. Lin et al. 2020), [O I] (A. J. McKay et al. 2020), OH (Z. Xing et al. 2020), and NH_2 (M. T. Bannister et al. 2020) species, and C_2, C_3, and CH reported in postperihelion observations (W. B. Hoogendam et al. 2026). 2I/Borisov had an unusually high abundance of CO (D. Bodewits et al. 2020; M. A. Cordiner et al. 2020) and Ni outgassing (P. Guzik & M. Drahus 2021; C. Opitom et al. 2021).

The recently discovered 3I/ATLAS is similar to 2I/Borisov: both showed cometary activity. D. Z. Seligman et al. (2025) reported initial signs of activity, which were confirmed by subsequent studies (M. A. Cordiner et al. 2025; R. de la Fuente Marcos et al. 2025; D. Jewitt et al. 2025; C. M. Lisse et al. 2025; C. Opitom et al. 2025; R. Rahatgaonkar et al. 2025; J. Tonry et al. 2025; C. O. Chandler et al. 2026; T. T. Frincke et al. 2026).

[7] NSF Graduate Research Fellow.
[8] NHFP Einstein Fellow.

Original content from this work may be used under the terms of the Creative Commons Attribution 4.0 licence. Any further distribution of this work must maintain attribution to the author(s) and the title of the work, journal citation and DOI.

The initial spectra exhibited red-sloped reflectance without strong emission features (C. Opitom et al. 2025; T. H. Puzia et al. 2025; D. Z. Seligman et al. 2025). As it approached perihelion, outgassing increased. Absorption from large water-ice grains in the coma (B. Yang et al. 2025) and emission from CN (R. Rahatgaonkar et al. 2025), HCN (I. M. Coulson et al. 2026; J. T. Hinkle et al. 2026), Ni (R. Rahatgaonkar et al. 2025; W. B. Hoogendam et al. 2026; D. Hutsemékers et al. 2026), Fe (D. Hutsemékers et al. 2026), CO_2 (M. A. Cordiner et al. 2025; C. M. Lisse et al. 2025), CO (M. A. Cordiner et al. 2025), and a likely extended source of OH emission (Z. Xing et al. 2025) has been reported.

Here, we present integral-field unit (IFU) observations of 3I/ATLAS from the Keck Cosmic Web Imager (KCWI; P. Morrissey et al. 2018) on the Keck II telescope. IFU data provide several advantages over slit spectroscopy, including no slit loss of photons and the ability to undertake studies using spatial as well as spectral information. Previous IFU data for 3I/ATLAS includes a spectrum from the SuperNova Integral Field Spectrograph (SNIFS; B. Lantz et al. 2004) presented in D. Z. Seligman et al. (2025). This spectrum was obtained as part of the Spectroscopic Classification of Astronomical Transients survey, which typically observes transient phenomena (e.g., M. A. Tucker et al. 2022, 2026). Further SNIFS observations are presented in a complementary study (W. B. Hoogendam et al. 2026). A spectrum from the Very Large Telescope (VLT)-mounted Multi Unit Spectroscopic Explorer (MUSE; R. Bacon et al. 2010), taken shortly after discovery, also shows cometary activity (C. Opitom et al. 2025). Unfortunately, the wavelength coverage of MUSE is not blue enough to observe the CN and Ni features discussed in this work.

2. Data

We obtained a KCWI spectrum on UTC 2025 August 24 06:06:49 (observation midpoint), along with two solar analogs and a flux calibration standard. 3I/ATLAS was at heliocentric and geocentric distances of 2.75 and 2.60 au, respectively, when our spectrum was taken. We used the small image slicer, providing an 8″ by 20″ field with a slice width of 0.″35. The blue channel used the BL grating, providing a spectral resolving power of $R \approx 3600$. The blue central wavelength was 4500 Å. The reliable wavelength coverage in the blue is from 3400 to 5500 Å. The total on-source integration time was 900 s. We reduced our KCWI data following standard `PypeIt` procedures (J. X. Prochaska et al. 2020b). We perform sky subtraction using the sky region from the standard star spectrum to prevent any self-subtraction of comet flux. We used calibration dome flats for flat-fielding and coadded the reduced, flux-calibrated cubes to create our final data cubes. `PypeIt` is not designed for nonsidereal objects, and the resulting flux calibration was disparate from the similar epoch (∼1 day difference) spectra from both UH88/SNIFS (which is spectrophotometric) (W. B. Hoogendam et al. 2026) and the VLT/XSHOOTER data from R. Rahatgaonkar et al. (2025). We correct our continuum flux to match these two other spectra (a factor of ∼10). We apply this correction to our spectrum and use the corrected flux values for subsequent analyses, since both instruments have well-calibrated reduction pipelines that have previously been used for nonsidereal objects. KCWI lacks a similarly well-tested pipeline for nonsidereal objects; this is the most accurate flux calibration we can obtain at this time. We extracted the spectrum using a 3″ aperture (beyond 3″, the aperture falls off the nearest chip edge). Figure 1 shows the 3400–5500 Å image from our KCWI spectrum.

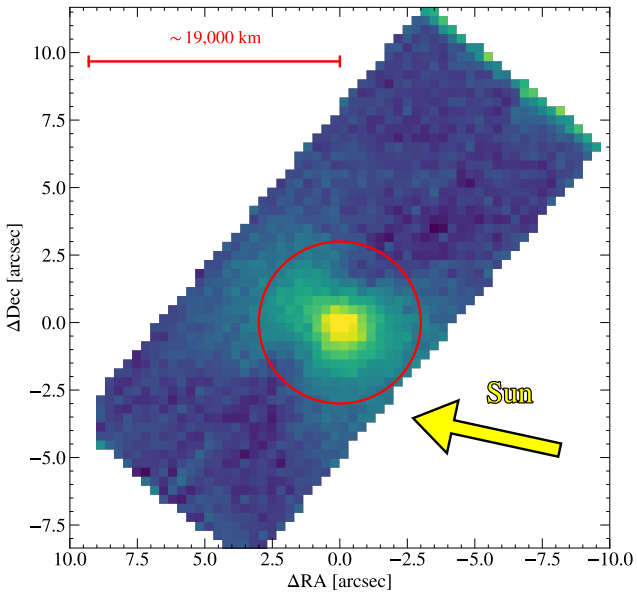

Figure 1. 3425–5500 Å white-light image from the KCWI data. The strap through the center of the comet is an instrumental residual that `PypeIt` was unable to remove. The scale bar is the physical scale of the comet viewed from Earth. The aperture is the 3″ aperture we used to extract our 1D spectrum. The yellow arrow denotes the direction to the Sun. The extended Sun-to-target radius vector is 102.°7.

3. Spectrospatial Analysis of 3I/ATLAS

To subtract the solar continuum contribution, we use HD 165290 as a solar analog. We model the continuum in the same manner as R. Rahatgaonkar et al. (2025). The model is defined as

$$F_{\rm cont}(\lambda) = R(\lambda) \times F_{\odot \rm analog}\left[\lambda\left(1 + \frac{v}{c}\right) + \delta\lambda\right], \quad (1)$$

where $R(\lambda) \equiv \frac{1}{S}(1 + b_1\lambda + b_2\lambda^2)$ is a second-order polynomial reflectance function normalized by a factor S that compensates for flux differences between the comet spectrum and solar analog spectrum, and $F_{\odot \rm analog}$ is the solar analog spectrum shifted by fitted free parameters v and $\delta\lambda$. v and $\delta\lambda$ are nuisance parameters that account for the relative motion between Earth and the comet and Earth and the solar analog star, or, in other words, fit residuals from velocity and dispersion differences between the solar analog spectrum and the true solar spectrum. The parameters b_1 and b_2 quantify the reflectance slope. The solar analog has a high signal-to-noise ratio, so the continuum-subtraction contribution to the error budget is negligible.

Figure 2 shows the 3425–4000 Å 1D continuum-subtracted spectrum from our KCWI data cube. Our spectrum extends to 5500 Å, but lacks spectroscopic features redward of 4000 Å (beyond CN).

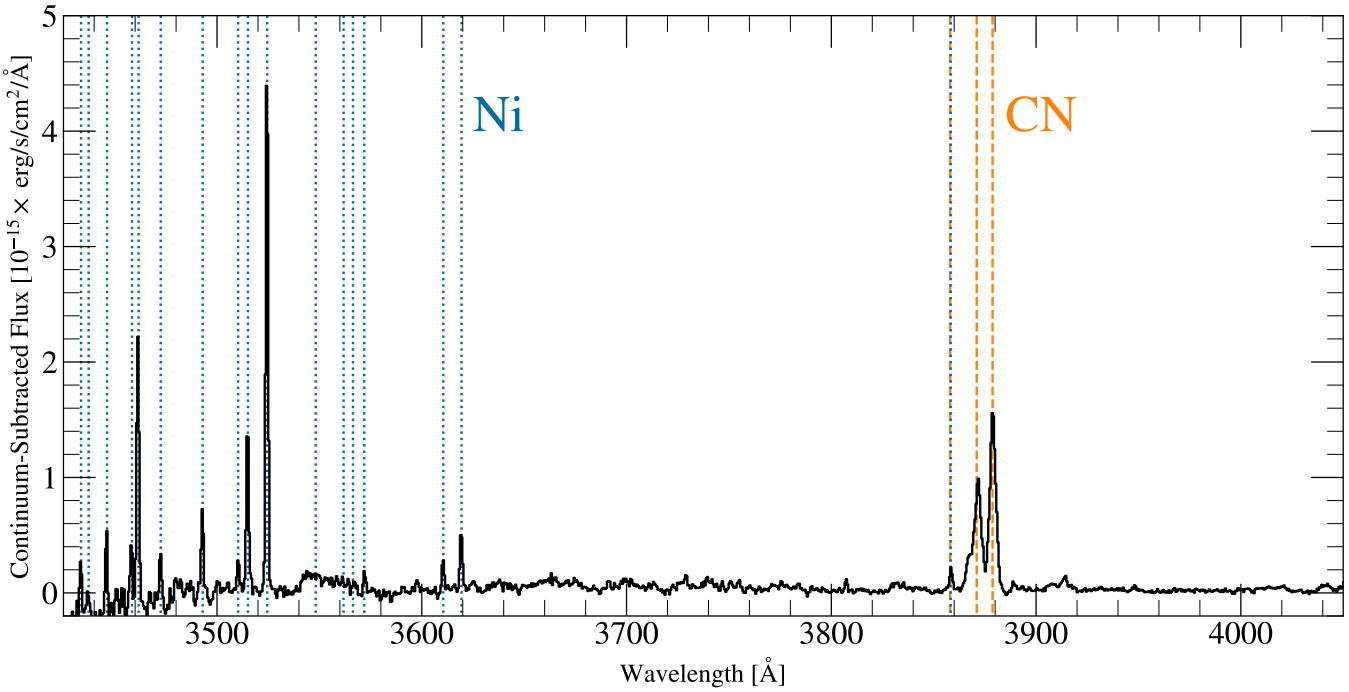

Figure 2. The continuum-subtracted KCWI spectrum of 3I/ATLAS between 3425 and 4050 Å, extracted from a 3″ aperture centered on the comet. The dotted blue and dashed orange lines denote Ni and CN, respectively. The emission feature at 3860 Å overlaps with both potential CN and Ni features. Given that the Ni transition at that wavelength is not expected to be particularly strong, we attribute that emission to CN.

3.1. Activity Signatures

We observe previously reported CN and Ni features (e.g., R. Rahatgaonkar et al. 2025). Fe I emission at ∼3722 and ∼3728 Å has previously been identified in comet Ikeya–Seki (1965f) by two independent studies (G. W. Preston 1967; C. D. Slaughter 1969) and other comets that also showed Ni I emission (J. Manfroid et al. 2021), but we do not see evidence for this feature in 3I/ATLAS in our spectrum (a later detection is reported by D. Hutsemékers et al. 2026). To place an upper limit on Fe emission in our spectrum, we insert a 3σ Gaussian emission feature. We use the sigma-clipped rms scatter of our continuum-subtracted spectrum as the 1σ value. The flux upper limit of the Fe I λ3720 feature is $F_{\rm Fe} = 9.9 \times 10^{-16}$ erg s^{-1} cm^{-2} Å^{-1}.

A simple (L. Haser 1957) model was used to convert the measured CN line flux into a gas production rate. The number of photons emitted per molecule per second (the so-called g-factor) and the scale lengths were taken from M. F. A'Hearn et al. (1995). We assumed that the gas escapes isotropically from the nucleus at a constant velocity, and adopted a mean expansion speed of $0.8 \times r^{-0.6}$ km s^{-1}, following N. Biver et al. (1999), where r is the heliocentric distance in astronomical units. The derived CN production rate is $Q(\mathrm{CN}) = (3.9 \pm 0.5) \times 10^{24}$ molecules s^{-1}.

3.2. Radial Distribution of CN and Ni

An advantage of our IFU data is the immediate availability of spectrospatial information about 3I/ATLAS. Slit-based techniques for studying radial distributions for comets involve dithering the slit between a central position and an offset position. Comet asymmetries in the coma may bias results from this technique, which has a limited field of view. Our data extend over 3″, or ∼5700 km, before the coma reaches the nearest chip edge. We leverage this unique data to analyze the spatial distribution of CN and Ni in 3I/ATLAS.

Figure 3 shows the KCWI 2D narrowband images of two similar-strength CN (left, from 3865 to 3885 Å) and Ni (right, from 3605 to 3625 Å) features. An extended coma is visible for CN, whereas the Ni emission has a more central profile. Figure 3 also shows anisotropy in the distribution of CN, with higher flux concentrations visible in both the sunward direction —where a dust plume has been observed in most observations of 3I/ATLAS since its discovery (M. A. Cordiner et al. 2025; D. Jewitt et al. 2025; D. Z. Seligman et al. 2025; C. O. Chandler et al. 2026)—and the antisunward direction, where antivelocity-directed cometary tails are spread out by a combination of radiation pressure and solar wind gas drag. 3I/ATLAS has indeed developed an antisolar tail as of late August.

The angular flux profile of 3I/ATLAS is shown in Figure 4. The left column shows the profile-subtracted data. The subtracted image reveals flux overdensities in the solar and antisolar directions. The perpendicular flux underdensities likely result from symmetric profile oversubtraction in those regions. The right column shows the azimuthal profiles calculated from the residual image maps.

The azimuthally averaged flux as a function of physical radial distance is shown in Figure 5. We bin the radial profiles into 1 pixel bins that correspond to ∼278 km given the pixel scale (0.″147 pixel^{-1}) and cometary distance. We normalize the flux to the maximum binned flux value. The Ni is more centrally concentrated than CN, with the majority of Ni flux coming from the innermost 2000 km of 3I/ATLAS. On the other hand, the radial profiles suggest that CN, though still concentrated near the nucleus, extends farther out into the coma.

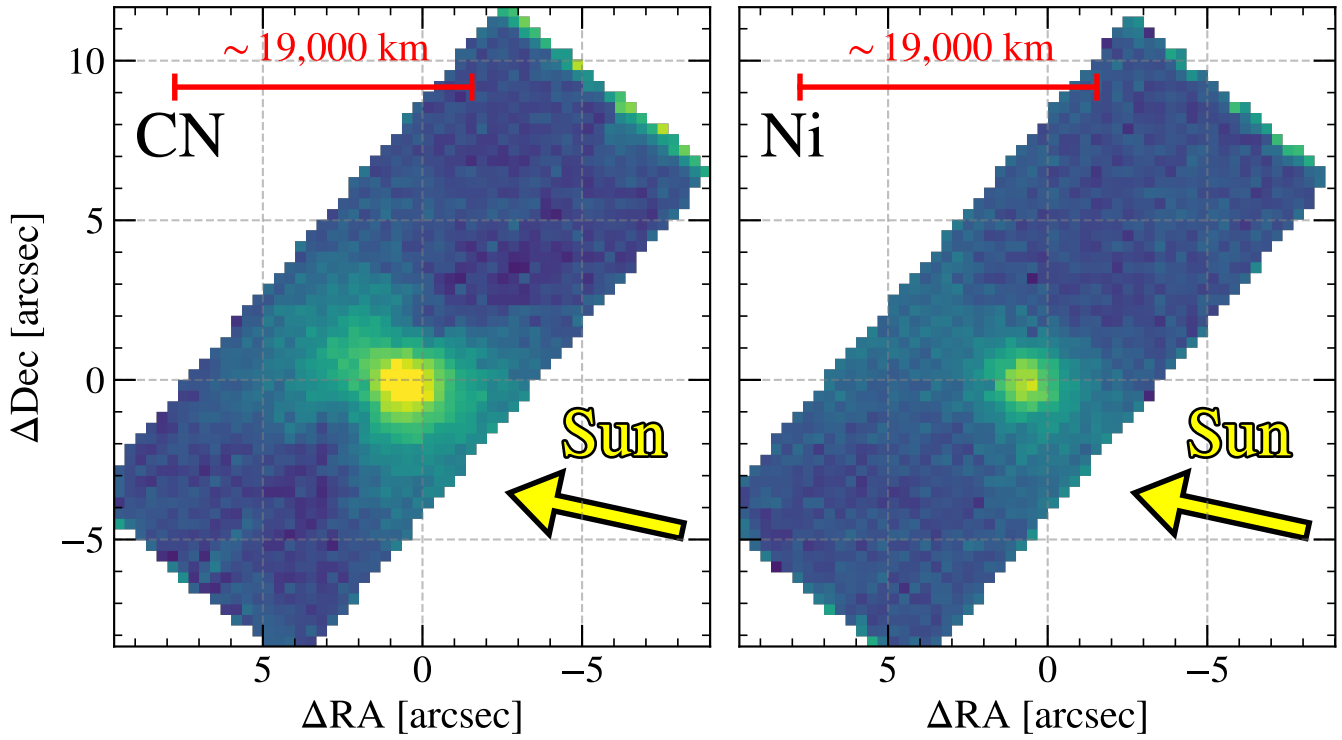

Figure 3. Comparison of narrowband images from the KCWI data cube for CN (left, from 3865 to 3885 Å) and Ni (right, from 3605 to 3625 Å). Both plots have a normalized color scale to account for differences in flux between the two lines. The scale bar is 10″.

We fit the radial profiles of CN and Ni with an exponential decay model defined as

$$A \times \exp\left[\frac{-x}{\tau}\right] + C \quad (2)$$

where τ is the characteristic e-folding length scale of the radial profile (and A and C are nuisance parameters). To account for differences in continuum level, we normalize the data to the maximum flux value. The fit is iterated 10 times; after each fit, outliers are sigma clipped, and the sigma-clipped data are refit. For Ni, we measure 593.7 ± 14.8 km (with $A = 1.233 \pm 0.034$ and $C = 0.006 \pm 0.002$), and for CN 841.0 ± 15.4 km (with $A = 1.028 \pm 0.018$ and $C = 0.010 \pm 0.002$).

4. Potential Physical Drivers of Ni Emission in Interstellar Comets

The recent work by R. Rahatgaonkar et al. (2025) discusses three possibilities for the Ni emission: metal carbonyls, such as $Ni(CO)_4$ and $Fe(CO)_5$, that are present in the comet (e.g., P. Guzik & M. Drahus 2021; J. Manfroid et al. 2021); metal–polycyclic aromatic hydrocarbons (PAHs; A. G. G. M. Tielens 2008) that photofragment and release Ni and PAHs; and a hybrid scenario (e.g., D. Brownlee et al. 2006; A. Bardyn et al. 2017) that invokes "in situ" formation of Ni carbonyls with Ni released from Ni sulfides. The radial distribution of Ni is a critical diagnostic to evaluate each scenario.

In the metal–carbonyl scenario, $Ni(CO)_4$ is more stable than its ferrous counterpart $Fe(CO)_5$ in the presence of water and oxidants. This enables trace $Ni(CO)_4$ to persist where $Fe(CO)_5$ would not, giving the observed Ni I emission without any Fe I counterpart. Additionally, $Ni(CO)_4$ quickly dissociates, which would result in a central concentration compared to other species, such as CN.

Metals such as Ni may attach to PAHs (A. G. G. M. Tielens 2008) to form Ni+PAH molecules (e.g., Ni-naphthalene, $Ni(C_{10}H_8)$, potentially). These molecules are easily unbound by absorbing light and may produce centrally concentrated Ni, as observed in 3I/ATLAS.

The hybrid scenario invokes UV sputtering or thermochemical erosion to produce Ni atoms from Ni sulfides such as $(Fe, Ni)_9S_8$. If the macroenvironment is CO-rich, then these sulfides carbonylate to $Ni(CO)_4$. The $Ni(CO)_4$ subsequently undergoes a similar photodissociation as the metal–carbonyl model described above. This "in situ" formation of $Ni(CO)_4$ predicts that Ni should be strongly concentrated near the nucleus, with potential anisotropies where dust jets intersect outflows of CO (e.g., P. Guzik & M. Drahus 2021). We observe a central Ni concentration; however, Figure 3 shows symmetric Ni emission. While M. A. Cordiner et al. (2025) reports a CO detection from James Webb Space Telescope data, compared to 2I/Borisov and other comets 3I/ATLAS is not CO-rich, and its distant activity was mostly driven by CO_2.

An emerging trend is that both 2I/Borisov and 3I/ATLAS appear to show is Ni/Fe ratios significantly above the solar value, as do the solar system comets in whose comas both metals have been measured at heliocentric distances too great for bulk refractory materials to sublime (J. Manfroid et al. 2021; C. Opitom et al. 2021). As discussed above, Fe-related carbonyls and PAH-based molecules may face greater obstacles to either formation, survival, or both, making them less common.

Another anomalous abundance is that of Fe/Ni relative to H_2O. 2I/Borisov (C. Opitom et al. 2021) and 3I/ATLAS are similar, based on the late-August ($r_h \approx 2.85$ au) Q(Ni) from R. Rahatgaonkar et al. (2025) and the $Q(H_2O)$ from

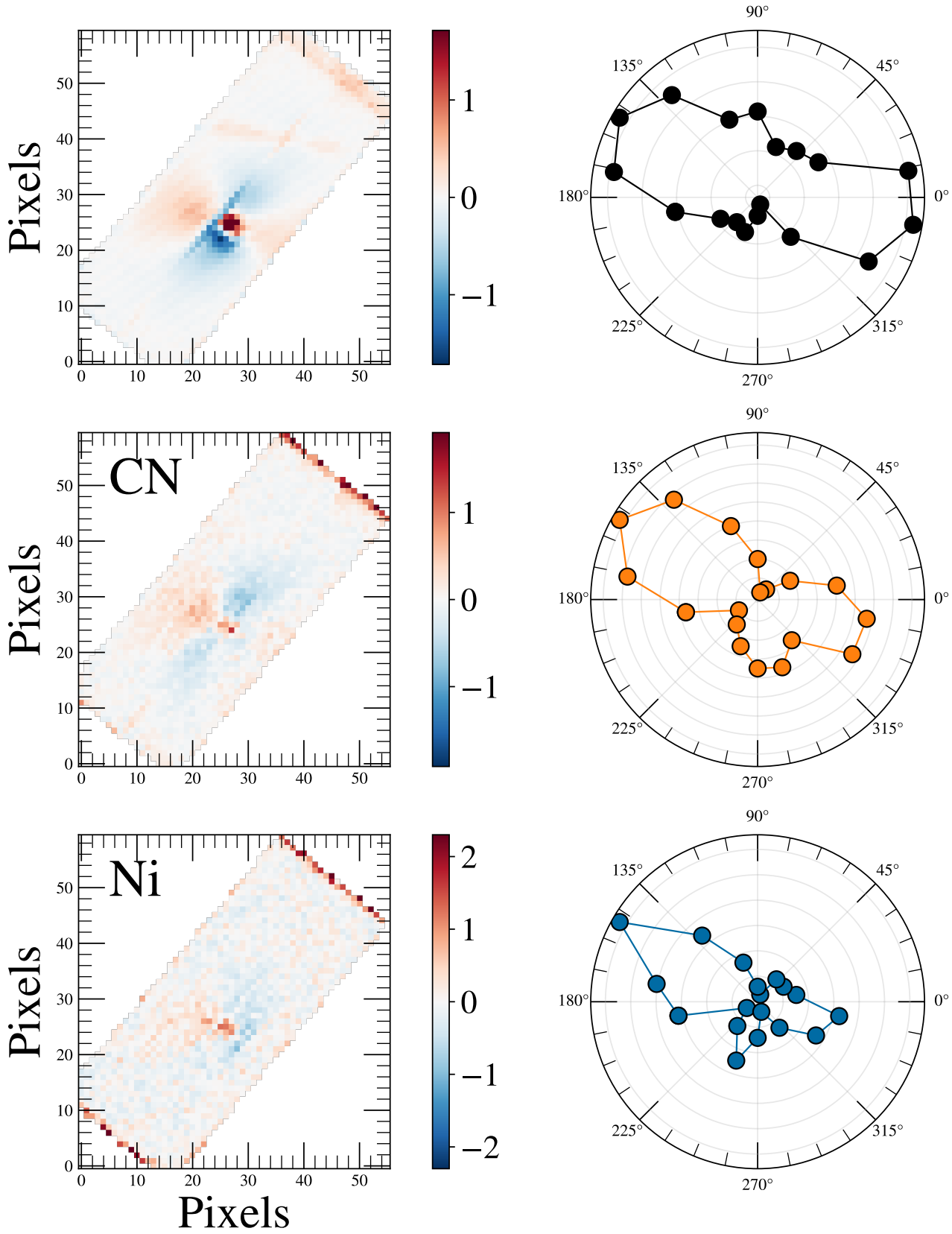

Figure 4. Determination of jets in the radial profiles of 3I/ATLAS. Left: model-subtracted data for white-light (top), CN (middle), and Ni (bottom) regions. Strong solar and antisolar flux excesses are visible in the broadband images. The flux values are rescaled to be near unity. Right: model-subtracted flux excess as a function of azimuth. The radial coordinate values are rescaled for each image; the extent of Ni emission is much more central than the broadband emission or CN, and the flux excess extends further for the broad band than for the CN and Ni.

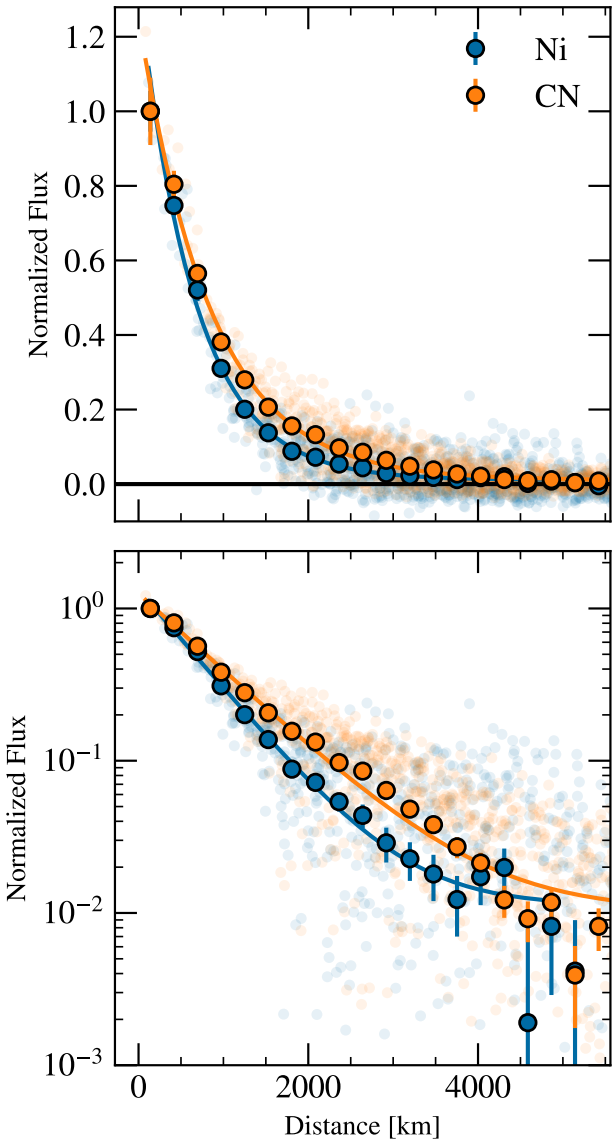

Figure 5. Measured radial differences between CN and Ni using the same ranges as Figure 3 in linear (top) and log (bottom) spacing. The maximum flux values for each feature are normalized to 1 to correct for (potential) differences in continuum luminosity. The sky background away from the comet is subtracted. Small points are the raw data, with larger, less transparent points showing the binned data. The lines are exponential functions fit to the data.

Z. Xing et al. (2025). While water ice can sublimate at this heliocentric distance, the activity in 3I/ATLAS at 2.85 au appears to be driven primarily by CO_2 rather than H_2O, as the sublimation flux of water ice at this distance may be insufficient to lift dust from the nucleus surface efficiently. Despite highly abundant CO, 2I/Borisov had a Q(Fe+Ni)/Q(CO) ratio that was similar to solar system comets (C. Opitom et al. 2021). Furthermore, comparing the R. Rahatgaonkar et al. (2025) Q(Ni) measured on August 9 (or July 31) with the Q(CO) measurement on August 6 from M. A. Cordiner et al. (2025), Q(Ni)/Q(CO) looks in line with the solar system trend (similar to 2I/Borisov), but Q(Ni)/Q(H_2O) looks ∼2 orders of magnitude higher, again similar to 2I/Borisov (C. Opitom et al. 2021).

The Q(Ni)/Q(CN) ratio from R. Rahatgaonkar et al. (2025) is ∼0.1, which is higher than 2I/Borisov and orders of magnitude above the solar system comet median (S. J. Bromley et al. 2021). This type of analysis, while only briefly discussed here, could help narrow down the source(s) of Fe and Ni in both solar system and interstellar comets and evaluate hypotheses for why these interstellar comets (so far) have different compositions (water-poorer relative to CO and CO_2) compared to a vast majority of solar system comets.

5. Conclusions

We present an IFU spectral analysis of the third interstellar comet 3I/ATLAS using data from Keck II/KCWI when 3I/ATLAS had a heliocentric distance of 2.75 au. We confirm previously reported CN and Ni activity, and measure the radial profiles of both CN and Ni, finding that the Ni emission is more centrally concentrated than the CN. Ni has a characteristic e-folding radius ∼200 km shorter than CN. This further supports a growing picture that Ni emission in comets arises from short-lived parent species, whose short lifetime is imprinted on the radial distribution of Ni. We also find evidence for asymmetric profiles for the broadband and CN and Ni narrowband images, with brighter integrated fluxes found to align with the solar and antisolar direction. This may be evidence for previously reported dust plumes in 3I/ATLAS (M. A. Cordiner et al. 2025; D. Jewitt et al. 2025; D. Z. Seligman et al. 2025; C. O. Chandler et al. 2026).

The presence of gaseous Ni in solar system comets and in 2I/Borisov and 3I/ATLAS suggests similarities between the unknown birthplaces or interstellar processing of the two latest interstellar interlopers and our own solar system. The lack of Fe emission in 3I/ATLAS differs from the solar system comets presented in J. Manfroid et al. (2021), P. Guzik & M. Drahus (2021), and 2I/Borisov (C. Opitom et al. 2021), but recent detections may indicate that Fe emission is triggered at closer heliocentric distances (D. Hutsemékers et al. 2026). This could provide new insights into how the chemistry, metallicity, and radiative evolution of stellar disks influence the formation and evolution of their small bodies.

The driving mechanism for Ni emission in the solar system and interstellar comets may differ, but independent of the physical driver, the measurement of Ni in a growing number of interstellar comets offers a promising pathway to trace the parent chemistry and metallicity of extrasolar planetary systems. Future IFU data will also provide spectrospatial information about the Fe radial distribution, enabling further comparative analysis between Fe, Ni, and other volatiles. The upcoming Legacy Survey of Space and Time (Ž. Ivezić et al. 2019) will discover and observe more interstellar comets, especially at greater heliocentric distances. As the number of these objects increases, population-level studies of the metal content in these objects and its dependence on heliocentric distance will be feasible, providing new insights into the extrasolar systems in which they form.

Acknowledgments

We thank Ryan Cooke for helpful discussions about KCWI reductions using PypeIt. We thank Thomas Puzia, Jaun Pablo Carvajal, John Noonan, and Cyrielle Opitom for helpful discussions about 3I/ATLAS and this work.

This work benefited significantly from the expertise and assistance of Keck Support Astronomer Greg Doppmann, who expedited access to the observing data and calibration files, and OA Julie Renaud-Kim, who was instrumental in getting

fast setups on nonsidereal targets working, enabling the efficient use of telescope time.

W.B.H. acknowledges support from the National Science Foundation Graduate Research Fellowship Program under grant No. 2236415.

K.J.M., J.J.W., and A.H. acknowledge support from the Simons Foundation through SFI-PD-Pivot Mentor-00009672. B.J.S, K.J.M, and W.B.H. acknowledge support from the NSF (AST-2407205) and NASA (HST-GO-17087, 80NSSC24K0521, 80NSSC24K0490, 80NSSC23K1431) grants.

J.T.H. acknowledges support from NASA through the NASA Hubble Fellowship grant HST-HF2-51577.001-A, awarded by STScI. STScI is operated by the Association of Universities for Research in Astronomy, Incorporated, under NASA contract NAS5-26555.

This research made use of `PypeIt`,[9] a Python package for semiautomated reduction of astronomical data (J. X. Prochaska et al. 2020a, 2020b).

ORCID iDs

Willem B. Hoogendam https://orcid.org/0000-0003-3953-9532
Benjamin J. Shappee https://orcid.org/0000-0003-4631-1149
James J. Wray https://orcid.org/0000-0001-5559-2179
Bin Yang https://orcid.org/0000-0002-5033-9593
Karen J. Meech https://orcid.org/0000-0002-2058-5670
Christopher Ashall https://orcid.org/0000-0002-5221-7557
Dhvanil D. Desai https://orcid.org/0000-0002-2164-859X
Kyle Hart https://orcid.org/0009-0003-2390-2840
Jason T. Hinkle https://orcid.org/0000-0001-9668-2920
Andrew Hoffman https://orcid.org/0000-0002-8732-6980
Esther M. Hu https://orcid.org/0009-0008-7427-4617
David O. Jones https://orcid.org/0000-0002-6230-0151
Kyle Medler https://orcid.org/0000-0001-7186-105X
Cameron M. Pfeffer https://orcid.org/0000-0002-7305-8321

References

A'Hearn, M. F., Millis, R. C., Schleicher, D. O., Osip, D. J., & Birch, P. V. 1995, Icar, 118, 223
Bacon, R., Accardo, M., Adjali, L., et al. 2010, SPIE, 7735, 773508
Bannister, M. T., Opitom, C., Fitzsimmons, A., et al. 2020, arXiv:2001.11605
Bardyn, A., Baklouti, D., Cottin, H., et al. 2017, MNRAS, 469, S712
Bessel, F. W. 1836, AN, 13, 185
Biver, N., Bockelée-Morvan, D., Crovisier, J., et al. 1999, AJ, 118, 1850
Bodewits, D., Bonev, B. P., Cordiner, M. A., & Villanueva, G. L. 2024, in Comets III, ed. K. J. Meech et al. (Univ. Arizona Press), 407
Bodewits, D., Noonan, J. W., Feldman, P. D., et al. 2020, NatAs, 4, 867
Borisov, G., Durig, D. T., Sato, H., et al. 2019, CBET, 4666, 1
Bromley, S. J., Neff, B., Loch, S. D., et al. 2021, PSJ, 2, 228
Brownlee, D., Tsou, P., Aléon, J., et al. 2006, Sci, 314, 1711
Chandler, C. O., Bernardinelli, P. H., Jurić, M., et al. 2026, ApJL, 1001, L35
Cordiner, M. A., Milam, S. N., Biver, N., et al. 2020, NatAs, 4, 861
Cordiner, M. A., Roth, N. X., Kelley, M. S. P., et al. 2025, ApJL, 991, L43
Coulson, I. M., Kuan, Y.-J., Charnley, S. B., et al. 2026, MNRAS, 546, stag063
Cowan, J. J., & A'Hearn, M. F. 1982, Icar, 50, 53
Cremonese, G., Fulle, M., Cambianica, P., et al. 2020, ApJL, 893, L12
de la Fuente Marcos, R., Alarcon, M. R., Licandro, J., et al. 2025, A&A, 700, L9
Denneau, L., Siverd, R., Tonry, J., et al. 2025, MPEC, 2025-N12
Do, A., Tucker, M. A., & Tonry, J. 2018, ApJL, 855, L10
Fitzsimmons, A., Hainaut, O., Meech, K. J., et al. 2019, ApJL, 885, L9
Fitzsimmons, A., Meech, K., Matrà, L., & Pfalzner, S. 2024, in Comets III, ed. K. J. Meech et al. (Univ. Arizona Press), 731
Frincke, T. T., Yaginuma, A., Noonan, J. W., et al. 2026, MNRAS, 545, staf1994
Guzik, P., & Drahus, M. 2021, Natur, 593, 375
Guzik, P., Drahus, M., Rusek, K., et al. 2020, NatAs, 4, 53
Haser, L. 1957, BSRSL, 43, 740
Hinkle, J. T., Yang, B., Meech, K. J., et al. 2026, OJAp, 9, 63250
Hoogendam, W. B., Jones, D. O., Yang, B., et al. 2026, ApJ, 1003, 245
Hoogendam, W. B., Kuesters, D., Shappee, B. J., et al. 2026, OJAp, 9, 65099
Hui, M.-T., Ye, Q.-Z., Föhring, D., Hung, D., & Tholen, D. J. 2020, AJ, 160, 92
Hutsemékers, D., Manfroid, J., Jehin, E., et al. 2026, A&A, 706, A43
Ivezić, Ž., Kahn, S. M., Tyson, J. A., et al. 2019, ApJ, 873, 111
Jewitt, D., Hui, M.-T., Mutchler, M., Kim, Y., & Agarwal, J. 2025, ApJL, 990, L2
Jewitt, D., & Luu, J. 2019, ApJL, 886, L29
Jewitt, D., Luu, J., Rajagopal, J., et al. 2017, ApJL, 850, L36
Jewitt, D., & Seligman, D. Z. 2023, ARA&A, 61, 197
Kim, Y., Jewitt, D., Mutchler, M., et al. 2020, ApJL, 895, L34
Lantz, B., Aldering, G., Antilogus, P., et al. 2004, SPIE, 5249, 146
Lin, H. W., Lee, C.-H., Gerdes, D. W., et al. 2020, ApJL, 889, L30
Lisse, C. M., Bach, Y. P., Bryan, S., et al. 2025, RNAAS, 9, 242
Manfroid, J., Hutsemékers, D., & Jehin, E. 2021, Natur, 593, 372
McKay, A. J., Cochran, A. L., Dello Russo, N., & DiSanti, M. A. 2020, ApJL, 889, L10
Meech, K. J., Weryk, R., Micheli, M., et al. 2017, Natur, 552, 378
Micheli, M., Farnocchia, D., Meech, K. J., et al. 2018, Natur, 559, 223
Morrissey, P., Matuszewski, M., Martin, D. C., et al. 2018, ApJ, 864, 93
Opitom, C., Fitzsimmons, A., Jehin, E., et al. 2019, A&A, 631, L8
Opitom, C., Jehin, E., Hutsemékers, D., et al. 2021, A&A, 650, L19
Opitom, C., Snodgrass, C., Jehin, E., et al. 2025, MNRAS, 544, L31
'Oumuamua ISSI Team, Bannister, M. T., Bhandare, A., et al. 2019, NatAs, 3, 594
Preston, G. W. 1967, ApJ, 147, 718
Prochaska, J. X., Hennawi, J., Cooke, R., et al. 2020a, pypeit/PypeIt: Release v1.0.0, Zenodo, doi:10.5281/zenodo.3743493
Prochaska, J. X., Hennawi, J. F., Westfall, K. B., et al. 2020b, JOSS, 5, 2308
Puzia, T. H., Rahatgaonkar, R., Carvajal, J. P., Nayak, P. K., & Luco, B. 2025, ApJL, 990, L27
Rahatgaonkar, R., Carvajal, J. P., Puzia, T. H., et al. 2025, ApJL, 995, L34
Seligman, D. Z., Micheli, M., Farnocchia, D., et al. 2025, ApJL, 989, L36
Slaughter, C. D. 1969, AJ, 74, 929
Tielens, A. G. G. M. 2008, ARA&A, 46, 289
Tonry, J., Denneau, L., Alarcon, M., et al. 2025, ApJL, 995, L15
Tonry, J. L., Denneau, L., Heinze, A. N., et al. 2018, PASP, 130, 064505
Trilling, D. E., Mommert, M., Hora, J. L., et al. 2018, AJ, 156, 261
Tucker, M. A., Huber, M. E., Shappee, B. J., et al. 2026, OJAp, 9, 69213
Tucker, M. A., Shappee, B. J., Huber, M. E., et al. 2022, PASP, 134, 124502
Whipple, F. L. 1950, ApJ, 111, 375
Whipple, F. L. 1951, ApJ, 113, 464
Xing, Z., Bodewits, D., Noonan, J., & Bannister, M. T. 2020, ApJL, 893, L48
Xing, Z., Oset, S., Noonan, J., & Bodewits, D. 2025, ApJL, 991, L50
Yang, B., Li, A., Cordiner, M. A., et al. 2021, NatAs, 5, 586
Yang, B., Meech, K. J., Connelley, M., & Keane, J. V. 2025, ApJL, 992, L9
Ye, Q., Kelley, M. S. P., Bolin, B. T., et al. 2020, AJ, 159, 77
Ye, Q.-Z., Zhang, Q., Kelley, M. S. P., & Brown, P. G. 2017, ApJL, 851, L5

[9] https://pypeit.readthedocs.io/en/latest/